Chemical Engineering Journal 323 (2017) 592–604

Contents lists available at ScienceDirect

Chemical Engineering Journal

journal homepage: www.elsevier.com/locate/cej

Verification of size-resolved population balance modeling for engineered nanoparticles under high concentration

Mingzhou Yu [a,b,c,*], Jianzhong Lin [a,d,*], Martin Seipenbusch [c], Junji Cao [b]

[a] China Jiliang University, Hangzhou 310018, China
[b] Institute of Earth Environment, Chinese Academy of Sciences, Xi'an 710075, China
[c] Institute for Mechanical Processes Engineering and Mechanics, Karlsruhe Institute of Technology, Germany
[d] Institute of Fluid Engineering, Zhejiang University, Hangzhou, China

HIGHLIGHTS

- The feasibility of PBM for characterizing size-resolved fractal-like ENPs under high concentration was studied.
- The crucial factors affecting the accuracy of the PBM for ENP were revealed.
- The Thajudeen et al.'s aggregate function was verified as the most accurate function as the PBM was implemented.

ARTICLE INFO

Article history:
Received 23 December 2016
Received in revised form 6 April 2017
Accepted 25 April 2017
Available online 28 April 2017

Keywords:
Size-resolved population balance modeling
Fractal-like aggregate
High concentration
Verification

ABSTRACT

Concerns have increased regarding the efficacy of population balance modeling (PBM) for determining the size-resolved behavior of engineered nanoparticles (ENPs) in chemical reactors, flames and workplaces. For the first time, we used a well-designed experiment to verify the feasibility of PBM and crucial factors affecting the accuracy of this method when size-resolved behavior was primarily concerned. The dynamic processes were designed to maximally represent high concentration involving aggregate production, deposition, coagulation, and transport. A population balance equation corresponding to the physical changes in an experiment was established and was further solved using the highly accurate moving sectional method. We verified four representative aggregate collision rate functions, namely the modified Fuchs collision rate function, Dahneke's collision function, harmonic mean collision function, and aggregate function newly developed by Thajudeen et al. (Aerosol Sci. Technol. 46 (2012) 1174–1186). The PBM implemented using the Thajudeen et al.'s aggregate function revealed highest agreement between the simulation and measurement. We observed both fractal dimension and primary particle diameter have apparent effects on the accuracy of PBM, indicating that both are key parameters in the implementation of PBM, whereas the pre-exponential factor only slightly affects the accuracy of PBM. The PBM with constant primary particle size, fractal dimension, and pre-exponential factor was finally verified as a reliable method for studying size-resolved evolution of ENPs over time.

1. Introduction

With the development of modern nanoparticle synthesis engineering [1–3], the numerical method for characterizing nanoparticle evolution from gas phase to product undergoes rapid development. Such particles are usually fractal-like aggregates composed of much smaller primary particles, with their diameters varying from approximately ~1 nm to ~1 μm [1,3]. From particle formation to grew particle, besides external processes such as convection and diffusion, there are several internal dynamics processes, including coagulation, production with nucleation mechanism or chemical react mechanism, sintering, and deposition [4]. The most suitable method describing this type of processes is population balance modeling (PBM), which is expected to capture the evolution of nanoparticle size distribution (PSD) through solving the coupled Navier-Stokes equations and population balance equation (PBE) [2,5–7]. However, there are many input parameters and functions which need to be specified with experiment or experiences in advance when implementing the PBM, such as coagulation kernel function and properties related

* Corresponding authors at: Zhejiang University, Hangzhou 310058, China (J. Lin); China Jiliang University, Hangzhou 310018, China (M. Yu).
E-mail address: yumingzhou1738@yahoo.com (M. Yu).

http://dx.doi.org/10.1016/j.cej.2017.04.128
1385-8947/

Nomenclature

d_f	Aggregate characteristic diameter
D_f	Fractal dimension of aggregates
k_f	The pre-exponential factor
d_{p0}	Primary particle diameter
d_{mv}	Mass equivalent diameter of the aggregate
$n(v,t)$	Particle number concentration with respect to particle volume v
v_{mv}	Mass equivalent volume of aggregates
d_m	Electric mobility diameter
$C(d_m)$	Slip correction for the aggregate mobility diameter
F_{in}, F_{out}	Air flow rate
V	Chamber volume
s	Constant production rate
v_{dv}, v_{du}, v_{dd}	Deposition velocities
A_v, A_u, A_d	Wall areas
u^*	Friction velocity
D_i	Diffusion coefficient
m_i	Particle mass
k_b	Boltzmann constant
T	Temperature
Kn	Knudsen number
c_u	CO_2 volume concentration

Greek symbols

λ	Mean free path of the gas
β	Coagulation kernel
$\in_d$	Deposition loss rate
v	Gas kinetic viscosity
μ	Air viscosity
σ_g	Geometric standard deviation

to nanoparticle morphology [7–10]. This results in some uncertain of the PBM. In fact, it is unclear to what extent PBM agrees with the experiment under high number concentration involving multiple physical changes, such as production release, coagulation, deposition, and transport. For the first time, this work was designed to verify the efficacy of PBM for grasping detailed PSD during nanoparticle evolution, and attempt to make clear crucial factors affecting the accuracy of this method. The dynamic processes were designed to maximally represent realistic high number concentration condition involving aggregate production, deposition, coagulation, and transport. To achieve the quantitative comparison of the evolving PSD between the PBM and experiment, the calculation for Navier-Stokes equation was not involved, which makes the comparison affected by uncertain as little as possible.

The Smoluchowski mean-field theory has been the fundamental theory for studying aerosol dynamics [11]. The key to this theory is its general but powerful governing equation [i.e., the PBE] [4]. The PBE is an integral–differential Fokker–Planck equation that considers the particle number intensity, and it can provide details of the evolution of the aerosol size distribution and statistical quantities, such as the total particle number and volume concentration, over time. Because of its inherent advantage of coupling to computational fluid dynamics within an Eulerian–Eulerian framework, the PBE and relevant modeling method (i.e., PBM) play an increasingly crucial role in both environmental and chemical engineering [12,13]. However, how to validate PBM by using a suitable experimental method remains unclear, particularly for tracing the evolution of size-resolved aggregate distribution over time in engineering condition. Currently, the most common method to validate a novel PBM model involves selecting a more accurate model as the reference. Notably, almost all studied PBM models, including the method of moments (MOM) and Monte Carlo, have used the sectional method (SM) as a reference because of its higher accuracy [7,14,15].

A major limitation of the aforementioned verification is that PBM is validated mathematically rather than physically. Thus, whether PBM provides realistic information on PSD evolution for fractal-like ENPs under high concentration and the extent to which PBM agrees with real physics are both unclear. In addition, the key factors affecting the reliability of PBM under realistic high emission scenarios are unknown. A comparative study of experiments and models under realistic scenarios condition typically has great potential to address these concerns. However, experiments with information identical to PBM are not easily practicable. The main difficulty is because of joint dynamical processes for aerosols that cannot be separated during the experimental measurements [8]. Under realistic high concentration, these aerosol dynamical processes include aggregate release or production, coagulation, deposition, and transport because of ventilation [16]. With the support of the Nanotransport Project by the European Commission under FP6, Seipenbusch et al. performed a comparative study of the temporal evolution of platinum ENPs in a simulated chamber by using both experiment and simulation but failed to provide the comparative information about aggregate size-resolved distribution because they used a highly simplified coagulation model [8]. Anand et al. proceeded to perform PBM modeling with the Fuchs collision rate according to Seipenbusch et al. experiment [17]; they only reported a qualitative comparison rather than a quantitative comparison between PBM and the measurement for size-resolved PSD during evolution; thus, their study could not examine the extent to which PBM agrees with real physics. In their PBM experiment, the pre-exponential factor was specified as 1.0; many researchers have verified this value as unsuitable for the diffusion-limited aggregate process [9,10]. The study verified this claim (Section 3.6). Although Rim et al. [18]conducted a comparative study on the sized-resolved evolution of indoor ultrafine particles by using both experiments and PBM simulation, they emphasized the assessment of the relative relevance of different dynamical processes under indoor aerosol concentrations, and their collision kernel was limited to the modified Fuchs model. The improved collision rate, such as that reported in Thajudeen et al.'s model [9] designed for fractal-like aggregates, was not used; thus, the reliability of such collision rate models when applied in resolving ENP dynamics remains unclear. Studies have reported relevance of the size-resolved study of aerosols; however, no study has focused on the evaluation of the feasibility of PBM for ENPs under high concentration.

Considering ENPs in chemical reactors or workplaces, the correct acquisition of appropriate numbers and short sudden emission events are crucial. High emission with high particle emission rate is the key characteristic of such events [8]. This is in contrast to common studies on indoor aerosols, where the total particle number is not high [18–20]. Because of the high particle number, coagulation might play a more critical role in determining the rapid change in PSD than other dynamics; thus, while implementing PBM, a highly reliable collision rate model for aggregates rather than for spherical particles is essential. Since the pioneering work of Fuchs for spherical particle collision over the entire size regime

[21], many collision models have been available for aggregates, such as the modified Fuchs model [22], Dahneke's collision model [23], and aggregate collision model developed by Thajudeen et al. [9]. According to our review of relevant literature, the Fuchs or modified Fuchs model is presently the most used collision version. Although Thajudeen et al. [9] claimed that the accuracy of PBM can be further increased with their model compared with other collision models, the claim has never been verified under realistic high number concentration.

Therefore, this comparative study, for the first time, verified the feasibility of PBM for characterizing size-resolved fractal-like ENPs under high concentration and addressed how well PBM can simulate the actual phenomenon and to what extent PBM agrees with the experiment under realistic high concentration conditions. Another objective of this study is to reveal crucial factors affecting the accuracy of this method when size-resolved behavior was primarily concerned. Here, we analyzed gold ENPs generated using a spark discharge generator. A moving SM was selected to model the size distribution evolution of the ENPs [17]. The study emphasized the evaluation of different aggregate collision kernels; determination of the most suitable collision function for ENPs; and analysis of the effects of the fractal dimension of the aggregates, pre-exponential factor, and primary particle size on the reliability of PBM. This paper is mainly divided into five sections. Section 1 introduces fractal-like ENP dynamics, research methods, and existing problems. Section 2 details the experiment and PBM. Section 3 presents and compares both experimental and modeled results. Sections 4 and 5 present the discussion and conclusions, respectively.

2. Materials and methods

2.1. Experimental setup and measurement

Fig. 1 shows a well-mixing chamber ($1 \times 1 \times 2\ m^3$) with a division plate A; the division plate divides the chamber into two equal zones. This chamber is at Karlsruhe Institute of Technology, Germany, and was originally designed for the Nanotransport Project by the European Commission under FP6 [8]. The division plate was designed to be installed or removed according to experimental requirements. Thus, the experiment can be performed inside zones

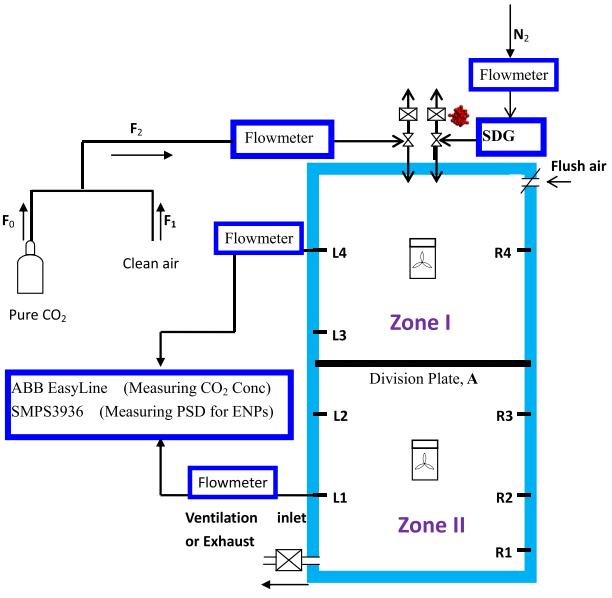

Fig. 1. Experimental setup.

I or (I + II, without a division plate). The zone (I + II) chamber was used in our previous dynamical studies on platinum nanoparticles, oil particles, and gold nanoparticles [17,24,25]. Turbulent mixing was achieved inside the zones by using fans with speeds controlled by adjusting the current. The sample ports were mounted over the chamber walls, and sampling was performed to measure the gold ENP size distribution. Real-time CO_2 concentration was measured to verify whether the aerosol mixed well inside zone I. Only the zone I chamber was used. Before the experiment, the air was flushed to clean the chamber so that the total particle number was maintained below 20 #/cm^3. The CO_2 concentration was measured using a continuous gas analyzers (EasyLine3020, ABB company, Germany).

Gold ENPs were produced using a self-made spark discharge generator according to a design reported by Schwyn et al. [26] The method for generating gold NPs was reported in our previous study [24]. The gold ENP carrier gas was nitrogen, with a volume flow of 4.0 lpm. The method can produce separated, unaggregated particles, 3–12 nm in diameter, and thus was highly suitable for studying fractal-like aggregate dynamics in this study [27]. In this study, we used a transmission electron micrograph (TEM) to obtain the statistical primary particle diameter (5 nm) and approximate mass fractional number of aggregates (1.75), which were used in the implementation of PBM. The chamber was vented with particle-free air between the experiments. The PSD time series was measured using a scanning mobility particle sizer (SMPS 3936, TSI model 3080 classifier with a TSI 0.071 cm pre-impactor). The measured data were corrected by both multiple charge particle correction and diffusion correction by using the TSI Aerosol Instrument Manager software. The PSD was measured at 135 s intervals to provide desirable time resolution. Notably, all measurement equipment, including the SMPS3936 and Easyline 3020, were calibrated before the experiment.

2.2. Population balance modeling

2.2.1. Population balance equation

The Kolmogorov turbulent vortex scale is approximately 1 μm in the air, and turbulent coagulation is negligible for particles smaller than 1 μm in characteristic diameter [4]. We referred to DeCarlo et al. [28] to define unambiguous particle diameter (or volume) and to systematize the relationships between different definitions. On the basis of the relationship of a power law (fractal-like) aggregate, the aggregate characteristic diameter d_f is expressed as follows

$$d_f = \frac{(d_{mv})^{\frac{3}{D_f}} (d_{p0})^{1-\frac{3}{D_f}}}{k_f} \quad (1)$$

here, D_f is the fractal dimension of aggregates in a statistical sense, and k_f is the pre-exponential factor; d_{p0} is the primary particle diameter, and d_{mv} is the mass equivalent diameter of the aggregate; it is the diameter of a spherical particle without void, which is obtained from fractal-like aggregates undergoing the coalescence process. In the PBM governing equation, as shown in Eq. (4), the internal coordinate of particle number function $n(v,t)$., volume v is specified as the mass equivalent vume of aggregates and allows the conservation of total aggregate volumes when implementing the SM, which can effectively ensure the accuracy of the numerical calculation of the method. To compare the measurement obtained from the SMPS 3936 and calculated data by solving Eq. (4), we must relate the mass equivalent volume (or diameter) and mobility volume (or diameter) as follows [29]:

$$v_{mv} = \frac{2\pi^2 \lambda d_{p0}}{c^*} \frac{d_m}{C(d_m)} \quad (2)$$

here, $v_{mv}$is the mass equivalent volume, $\lambda$is the mean free path of the gas (68.41 nm in this study), and d_m is the electric mobility diameter accounting for the interaction between moving aggregates and their surrounding medium. In this study, we used the Aerosol Instrument Manager® Software (version 8.0) for TSI Model 3936 series SMPS™ spectrometer for the slip correction for the aggregate mobility diameter [30,31],

$$C(d_m) = 1 + \frac{2\lambda}{d_m}\left(1.142 + 0.558\exp\left(-\frac{1.998 d_m}{\lambda}\right)\right) \quad (3)$$

For aggregates oriented parallel to their relative motion, the dimensionless drag force, c^*, is 6.62, as was used by Lall et al. for silver aggregates [29]. For a comparative study, the aggregate number considering the mobility diameter was converted to aggregate number considering the aggregate mass equivalent volume. In this study, Eq. (2) was used to produce particle mobility diameter shown in Figs. 7–10 for all aggregation functions for comparative studies. Note that Eq. (12) should generate more reasonable relation between particle mobility size and mass equipment size for the Thajudeen et al.'s aggregation function.

A population balance model for the dynamical evolution of gold ENPs in a ventilated chamber with a constant injection rate was established according to the Smoluchowski mean-field theory [11,32]. In this study, gold ENPs inside the chamber were subjected to internal processes, including coagulation and production, and the external processes of deposition and ventilation. The governing PBE for the gold ENPs involving all relevant dynamical processes contributed to the size-resolved evolution of aggregates and is expressed as follows:

$$\frac{\partial n(v_{mv},t)}{\partial t} = \underbrace{\frac{1}{2}\int_0^{v}\beta(v_{mv}-v'_{mv},v'_{mv})n(v_{mv}-v'_{mv},t)n(v'_{mv},t)\,dv'_{mv} - n(v_{mv},t)\int_0^{\infty}\beta(v_{mv},v'_{mv})n(v'_{mv},t)\,dv'_{mv}}_{\text{coagualtion}} - \underbrace{\frac{F_{out}}{V}n(v_{mv},t)}_{\text{ventaltion}}$$
$$+ \underbrace{\frac{s(v_{mv},t)F_{in}}{V}}_{\text{producation}} + \underbrace{\frac{\epsilon_d(v_{mv})}{V}n(v_{mv},t)}_{\text{deposition}} \quad (4)$$

where $n(v_{mv},t)dv_{mv}$ is the number of particles with a physical volume (or mass equivalent volume) between v_{mv} and $v_{mv}+dv_{mv}$ at time t;$\beta(v_{mv},v'_{mv})$ is the collision kernel for two aggregated particles of physical volumes v_{mv} and v'_{mv}; $s(v_{mv})$ is the constant production rate independent on time t; ϵ_d is the deposition loss rate for aggregate with respect to volume, v_{mv}. F_{in} and F_{out} are the air flow rate because of the injection and exit, respectively, and were the same in this study; V is the chamber volume. For the zone I chamber, V is 1 m^3. This is a Fokker–Planck-type equation and allows tracking the evolution of the PSD over time, as long as some proper quantities or formulae, such as β, s, and ϵ_d, are available.

2.2.2. Deposition loss rate

This study obtained the particle loss rate coefficient of deposition by using Lai and Nazaroff's model [33]. The deposition loss rate coefficient is expressed as follows

$$\epsilon_d = \frac{v_{dv}A_v + v_{du}A_u + v_{dd}A_d}{V} \quad (5)$$

Where $v_{dv} = \frac{u^*}{1}$, $v_{du} = \frac{v_s}{1-\exp\left(-\frac{v_s l}{u^*}\right)}$, and $v_{dd} = \frac{v_s}{\exp\left(\frac{v_s l}{u^*}\right)-1}$ and v_{dv}, v_{du}, and v_{dd} are the deposition velocities on the vertical, upward horizontal, and downward horizontal surfaces; respectively; A_v, A_u, and A_d are the areas of these three surfaces. u^* is the friction velocity at the concentration boundary. The integral variable I is expressed as $I = \int_{r^+}^{30}\left(\frac{v}{\varepsilon_p+D}\right)dy^+$, where $r^+ = \left(\frac{d_m}{2}\right)(u^*/v)$; d_m is the particle mobility diameter, which needs to be converted from v_{mv} (d_{mv}) by using Eq. (2); v is the gas kinetic viscosity. For this model, the key is to specify the friction velocity u^*. In this study, we followed the approach used in our previous study to specify u^*, an averaged method based on data measured using SMPS 3936 [24,25], which is discussed in detail in Section 3.3. Notably, this averaged method was verified to yield the same results as the least square method, which was first developed by Hussein and et al. [19].

2.2.3. Collision rate function

The theoretical examination of the development of ENPs through particle–particle collision is difficult because aggregate collision dynamics is governed by more factors than spherical particles, including the aggregate structure, primary particle size, and aerosol volume loading. Thus, many versions of nonspherical aggregate collision kernels have been proposed since the pioneering work of Fuchs (1964) [21], which inevitably results in confusion for users during selection. In this study, we selected four predominantly used aggregate collision kernels and subsequently evaluated the most suitable kernel for studying ENP dynamics. These aggregate collision rates are the modified Fuchs collision model [34], Dahneke's transition regime collision model [23], harmonic mean collision model, and model for all diffusive Knudsen numbers developed by Thajudeen et al. [35] These models were designed for particle collision over the entire size regime covering

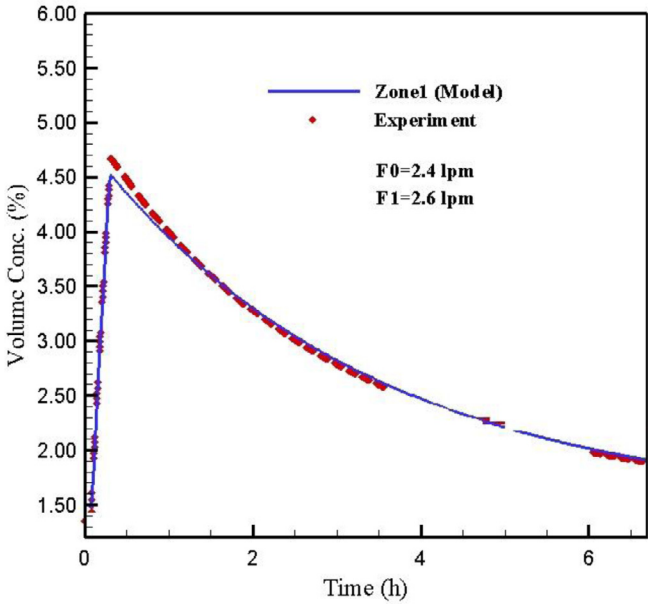

Fig. 2. Comparison of the measured and theoretical CO_2 volume over the time inside the zone I chamber.

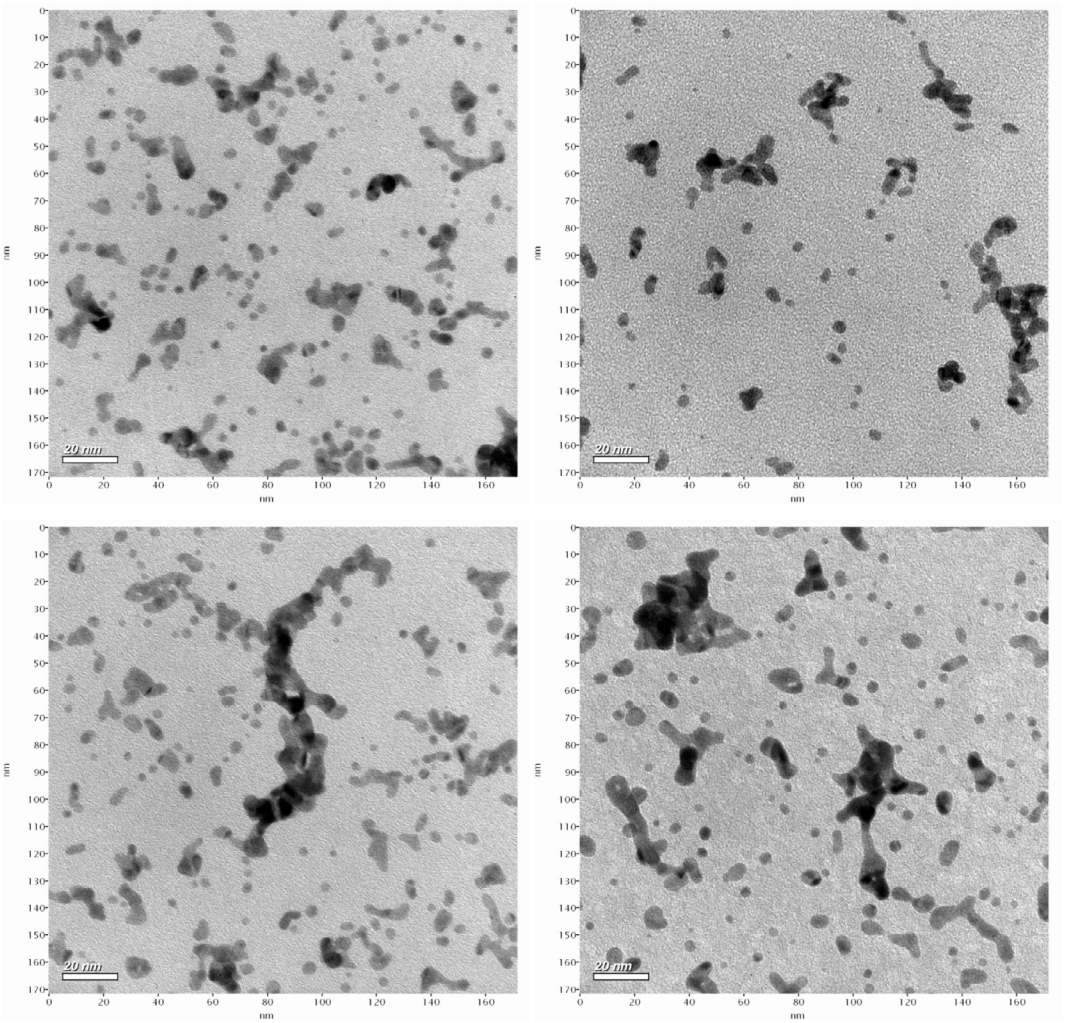

Fig. 3. TEM of gold ENPs generated using a spark discharge generator.

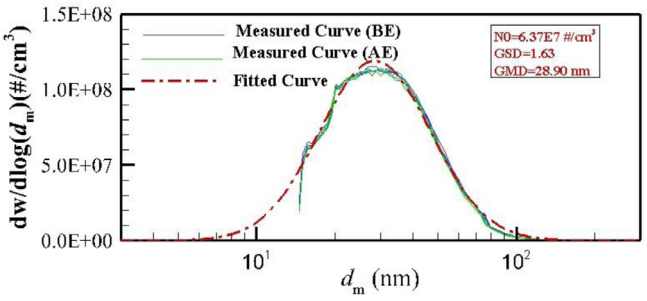

Fig. 4. PSD determined from the measurement and fit through the least square approximation method for the source.

the free molecular to continuum regimes, thus being insensitive to the aggregate size.

1. Modified Fuchs coagulation kernel

Fuchs's particle–particle collision expression is one of the most widely used expressions for β calculation for spherical particles. This expression was modified by researchers for fractal-like aggregates [34], in which collision and mobility sizes are differentiated as follows:

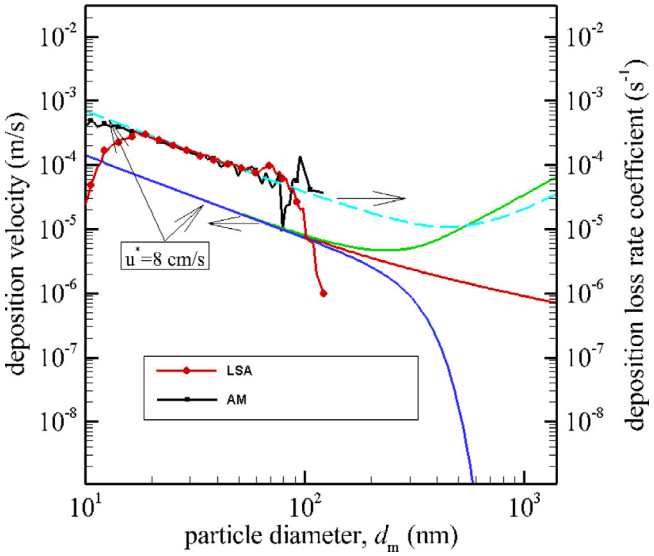

Fig. 5. Loss rate coefficient of gold ENP deposition obtained through the averaged method (AM) and least square approximation (LSA) method. The Lai and Nazaroff's theoretical model (2000) is presented for fitting the AM curve with friction velocity 8 cm/s.

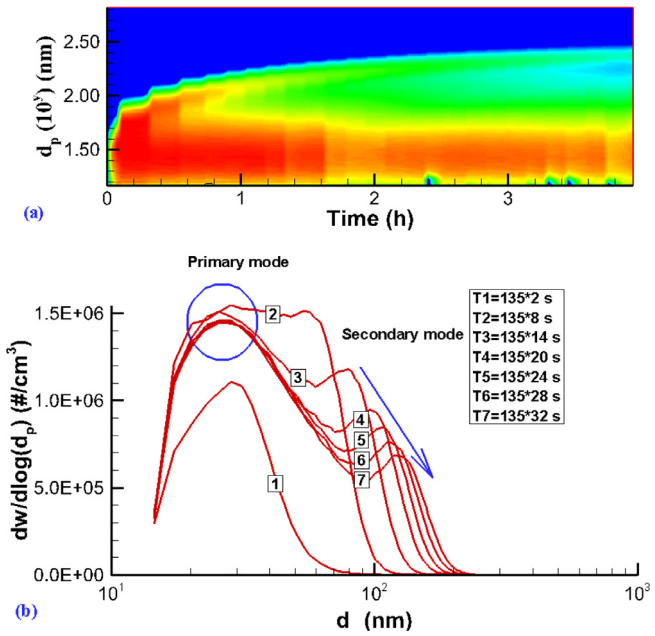

Fig. 6. Gold ENP evolution in the zone 1 chamber, as measured using SMPS3936.

$$\beta(\mathrm{i,j}) = 2\pi(D_\mathrm{i}+D_\mathrm{j})\left(d_{\mathrm{c_i}}+d_{\mathrm{c_j}}\right)\left(\frac{d_{\mathrm{c_i}}+d_{\mathrm{c_j}}}{d_{\mathrm{c_i}}+d_{\mathrm{c_j}}+2\left(g_\mathrm{i}^2+g_\mathrm{j}^2\right)^{1/2}}+\frac{8(D_\mathrm{i}+D_\mathrm{j})}{\left(\bar{c}_\mathrm{i}^2+\bar{c}_\mathrm{j}^2\right)^{1/2}(d_{\mathrm{c_i}}+d_{\mathrm{c_j}})}\right)^{-1} \quad (6)$$

where

$$\bar{c}_\mathrm{i} = \left(\frac{8k_\mathrm{b}T}{\pi m_\mathrm{i}}\right)^{1/2}$$

$$l_\mathrm{i} = \frac{8D_\mathrm{i}^\mathrm{a}}{\pi\bar{c}_\mathrm{i}}$$

$$g_\mathrm{i} = \frac{1}{3D_\mathrm{i}l_\mathrm{i}}\left[\left(d_{\mathrm{c_i}}+l_\mathrm{i}\right)^3-\left(d_{\mathrm{c_i}}^2+l_\mathrm{i}^2\right)^{3/2}\right]-d_{\mathrm{c_i}}$$

$$D_\mathrm{i} = \frac{k_\mathrm{b}TC_\mathrm{c}(d_{\mathrm{m,i}})}{3\pi\mu d_{\mathrm{m,i}}}$$

D_i is the diffusion coefficients for particles with the mobility diameter d_m and mass m_i; k_b is the Boltzmann constant, T is the temperature, and μ is the air viscosity. We followed a previously reported method [22,36]; let $d_\mathrm{c} = d_\mathrm{f}$, namely the collision diameter is obtained from the fractal theory for power law aggregates, and a = 1. Similar studies have reported the calculation for agglomerate dynamics [37]. The key modification of Fuchs expression the replacement of the diameter with the collision diameter in the collision kernel and with the mobility diameter in the diffusivity expression.

2. Dahneke's model and harmonic mean collision model

To improve the accuracy of Fuchs expression for characterizing the collision rate over the entire size regime, Dahneke accepted the idea of adsorbing spheres reported by Fuchs; however, he described the diffusion processes as a mean free path phenomenon [23,38]. Dahneke's collision model can be expressed as an enhancement of the collision function for the near-continuum regime.

$$\beta(\mathrm{i,j}) = 2\pi(D_\mathrm{i}+D_\mathrm{j})\left(d_{\mathrm{c_i}}+d_{\mathrm{c_j}}\right)\mathrm{f(Kn)} \quad (7)$$

here, the diffusion coefficient D and collision diameter d_c can be implemented as the same as in Eq. (6) for fractal-like aggregates. The enhancement function $f(\mathrm{Kn})$ is expressed as follows,

$$\mathrm{f(Kn)} = \frac{1+\frac{2}{3}\mathrm{Kn}}{1+\frac{4}{3}\mathrm{Kn}+\frac{8}{9}\mathrm{Kn}^2} \quad (8)$$

where the Knudsen number and classic mean free path definition, $\mathrm{Kn} = 2\lambda_\mathrm{p}/d_{12}$, $\lambda_\mathrm{p} = 3D_{12}/\bar{c}_{12}$, $d_{12} = d_1 + d_2$,$\bar{c}_{12} = \bar{c}_1 + \bar{c}_2$. Here, the aggregate diameter was specified as the mobility diameter, which is consistent with the definition in Eq. (6). As the enhancement function, $f(\mathrm{Kn})$ is expressed as follows:

$$\mathrm{f(Kn)} = \frac{1}{1+\frac{4}{3}\mathrm{Kn}} \quad (9)$$

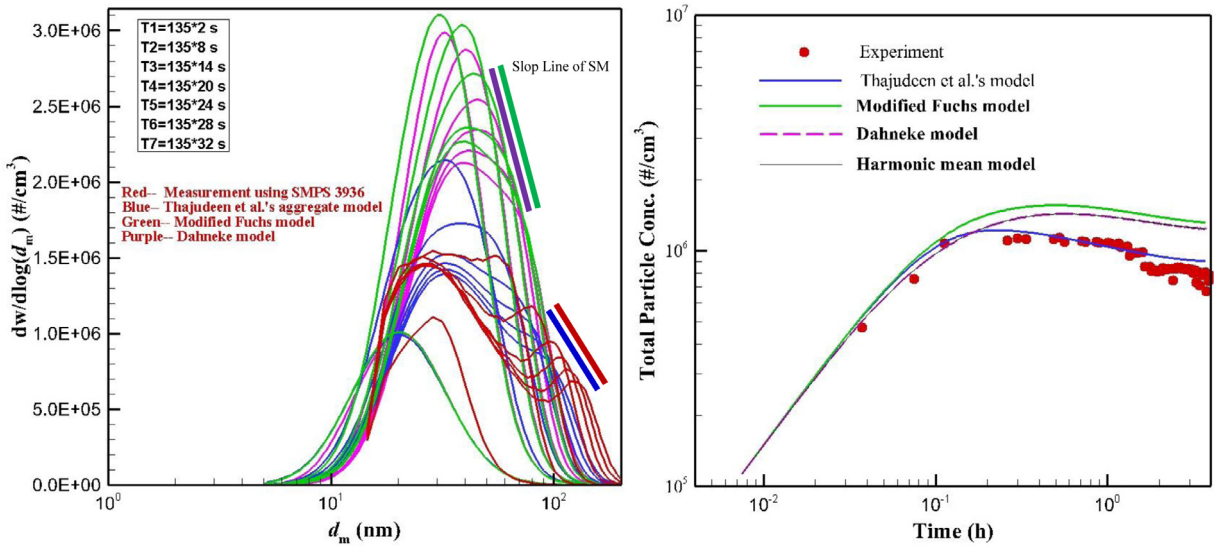

Fig. 7. Comparison of the size distribution evolution over time (a) and total aggregate number (b) between the experiment and PBM. The measurement data (red) are same as that in shown in Fig. 6. (For interpretation of the references to colour in this figure legend, the reader is referred to the web version of this article.)

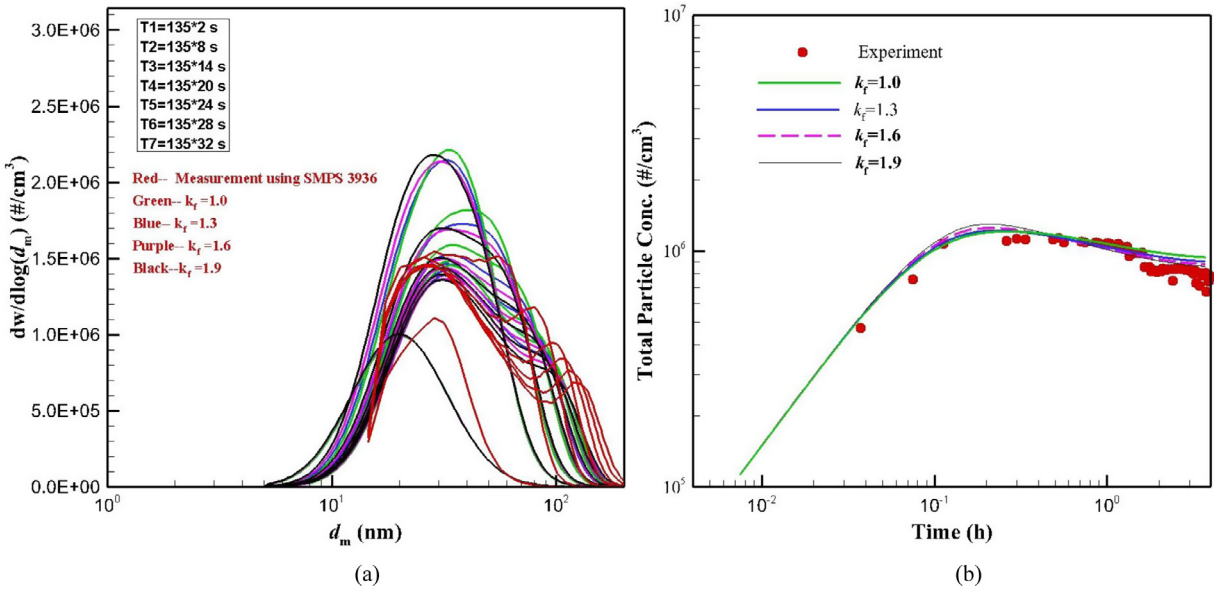

Fig. 8. Effects of the pre-exponential factor on the size distribution evolution over time and total particle number on using the aggregate collision model.

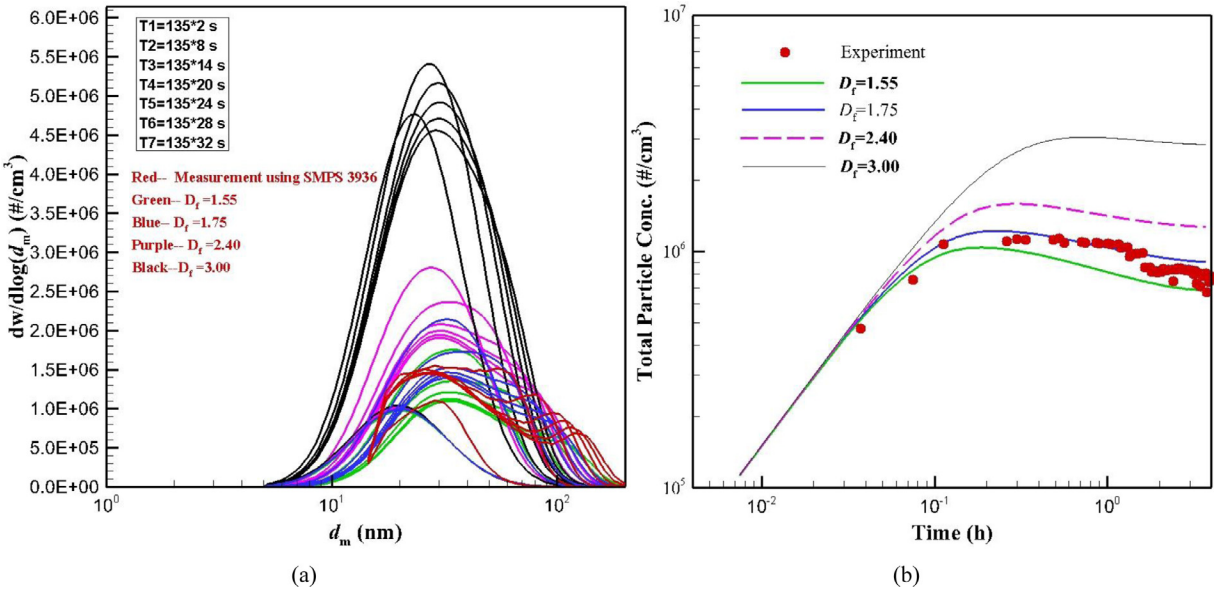

Fig. 9. Effects of the fractal dimension on the size distribution evolution over time and total particle number on using the aggregate collision model.

Eq. (7) shows the harmonic mean coagulation kernel, which is also a widely used collision rate model because of its simple mathematical expression [39].

3. Thajudeen et al.'s model

Recently, Thajudeen et al. developed a novel promising collision rate model on the basis of theoretical and numerical studies, which allows determining the transition regime collision rate for shaped aggregates [35,40–43]. In their study, Brownian Dynamics/Langevin Dynamics and Monte Carlo simulations were carried out. For quasifractal aggregates composed of monodisperse primary particles that are similar in size, regression relations were developed that enable calculation of the collision kernel directly from the quasifractal descriptors. The authors claimed that their model highly ensures the accuracy of PBM for aggregates. Thus, this model might be more suitable than others for determining the evolution of size-resolved ENPs. The collision rate function is expressed as follows,

$$\beta(\mathrm{i},\mathrm{j}) = \frac{Hf_{\mathrm{ij}}\mathrm{PA}_{\mathrm{ij}}^2}{\pi^2 m_{\mathrm{ij}} R_{\mathrm{s,ij}}} \tag{10}$$

where m_{ij} and f_{ij} are the reduced mass and scalar friction factor for i and j, $\frac{1}{m_{\mathrm{ij}}} = \frac{1}{m_{\mathrm{i}}} + \frac{1}{m_{\mathrm{j}}}$ and $\frac{1}{f_{\mathrm{ij}}} = \frac{1}{f_{\mathrm{i}}} + \frac{1}{f_{\mathrm{j}}}$. The friction factor is expressed as follows,

$$f_{\mathrm{i}} = \frac{6\pi\mu R_{\mathrm{S,i}}}{1 + \mathrm{Kn}(1.257 + 0.4\exp[-\frac{1.1}{\mathrm{Kn}}])} \tag{11}$$

with a new definition of the Knudsen number $\mathrm{Kn} = \frac{\lambda\pi R_{\mathrm{S,i}}}{\mathrm{PA_i}}$. The Smoluchowski radius, $R_{\mathrm{S,i}}$, for aggregate i, is expressed as

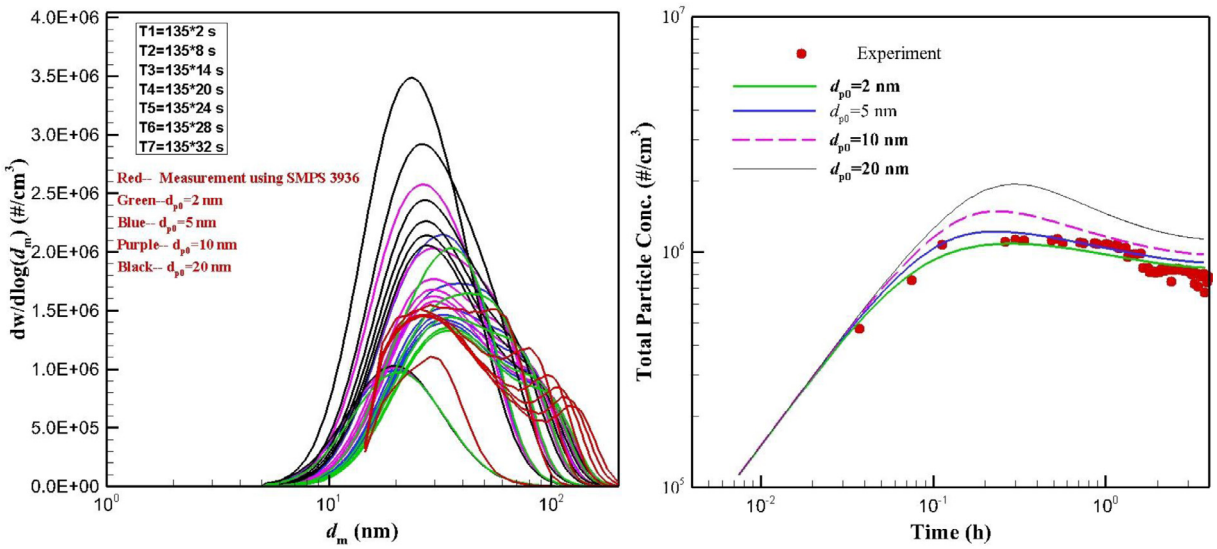

Fig. 10. Effects of the primary particle size on the aggregate size distribution evolution over time and total particle number on using the aggregate collision model.

$$\frac{R_{S,i}}{a_{p0}} = \Phi_R \left(\frac{N_i}{k_{f,i}}\right)^{1/D_{f,i}} \tag{12}$$

with

$$\Phi_R = \frac{1}{\alpha_1 \ln[N_i] + \alpha_2}$$

$$\alpha_1 = 0.253D_{f,i}^2 - 1.209D_{f,i} + 1.433$$

$$\alpha_2 = -0.218D_{f,i}^2 + 0.964D_{f,i} - 0.180$$

and the orientationally averaged projected area, PA_i, for aggregate i, is expressed as

$$\frac{PA_i}{\pi a_{p0}^2} = \Phi_P \left(\frac{N_i}{k_{f,i}}\right)^{\frac{2}{D_{f,i}}} \tag{13}$$

with

$$\Phi_P = \frac{N_i^{-\alpha_3}}{\alpha_4}$$

$$\alpha_3 = 0.439D_{f,i}^2 - 2.221D_{f,i} + 2.787$$

$$\alpha_4 = -0.232D_{f,i}^3 + 1.273D_{f,i}^2 - 2.183D_{f,i} + 1.906$$

The combined Smoluchowski radius, $R_{S,ij}$, for the collision of aggregates i and j is expressed as follows:

$$\frac{R_{S,ij}}{a_{p0}} = \left[1.203 - \frac{0.4315(N_i + N_j)}{(N_i D_{f,i} + N_j D_{f,j})}\right] \times \left(\frac{R_{S,i}}{a_{p0}} + \frac{R_{S,j}}{a_{p0}}\right)^{\left(0.8806 + \frac{0.3497(N_i+N_j)}{N_i D_{f,i} + N_j D_{f,j}}\right)} \tag{14}$$

The combined orientationally averaged projected area PA_{ij} is expressed as follows:

$$PA_{ij} = \pi R_{S,ij}^2 \tag{15}$$

here, N_i is the number of primary particles for aggregate i and $a_{p0} = \frac{1}{2}d_{p0}$. This model was designed for determining the transition regime collision rate for aggregates as the function of the fractal descriptors for each aggregate. In this study, we considered $D_{f,i} = D_{f,j}$ and $k_{f,i} = k_{f,j}$ to agree with the requirement of PBM, in which all aggregates are approximated to have the same fractal properties.

2.2.4. Sectional method

The SM was introduced to solve Eq. (4). The SM effectively divides the PSD into bins and can trace the PSD evolution with high accuracy; thus, it has been widely used to study aerosol dynamics and as an exact method to verify other methods, such as the MOM [15]. Each bin has a governing ordinary differential equation (ODE) considering the particle number, which can be solved using general numerical methods for solving ODEs, such as the Runge–Kutta method with a fixed or varied time step [14].

Introducing the SM into Eq. (4) yields the following equation:

$$\frac{d\tilde{N}_k}{dt} = \underbrace{\omega_k}_{\text{coagualtion}} - \underbrace{\frac{F_{out}}{V}\tilde{N}_k}_{\text{ventilation}} + \underbrace{F_{in}\frac{S_k}{V}}_{\text{production}} + \underbrace{\frac{\lambda_d}{V}\tilde{N}_k}_{\text{deposition}} \tag{16}$$

where

$$\omega_k = \begin{cases} -\tilde{N}_1 \sum_{i=1} \beta_{i1}\tilde{N}_i; \ k = 1 \\ \frac{1}{2}\sum_{\substack{i=1 \\ j=1}} \chi_{ijk}\beta_{ij}\tilde{N}_i\tilde{N}_j - \tilde{N}_k \sum_{i=1} \beta_{ik}\tilde{N}_i; \ k > 1 \end{cases}$$

where

$$\chi_{ijk} = \begin{cases} \frac{v_{k+1} - (v_i + v_j)}{v_{k+1} - v_k}; \ \text{if } v_k \leqslant v_i + v_j \leqslant v_{k+1}, \\ \frac{(v_i + v_j) - v_{k-1}}{v_k - v_{k-1}}; \ \text{if } v_{k-1} \leqslant v_i + v_j \leqslant v_k, \\ 0; \text{else} \end{cases}$$

and $\tilde{N}_k = \int_{v_k}^{v_{k+1}} n(v,t)dv$, v_k and v_{k+1} correspond to the low and high particle volume limits, respectively, at bin k.

For SM performance, the bin node positions were always moved according to the specific range in which most ENPs were dominant; however, the total number of bins was preserved. The fourth-order Runge–Kutta method was used a fixed time step to solve the set of ODEs, and the error function in the moving SM was computed using the incomplete Gamma function method. The time step for the moving SM was 2.7 s for all computations.

The total section number was 200, and the space factor for the sections was 1.08. During the modeling, the temperature and pressure of the surrounding air was assumed to be 300 K and 1.013 × 105 Pa, respectively, which is identical to the experimental conditions. In this case, the viscosity and mean free path of the gas molecules were $1.850\,772 \times 10^{-5}$ Pa s and 68.41 nm, respectively. The gold ENP morphology was assumed to be fractal-like, with a fractal dimension of 1.75, same as that in a previous study [17]. The determination of fractal dimension of fractal-like aggregates will be shown in Section 3.2.

3. Results and discussions

3.1. Verification of the well-mixed conditions

This study used CO_2 as a tracer gas to verify whether aerosols mix well on being injected into the chamber, otherwise the PBE, as shown in Eq. (4), cannot be used in this study. Unlike gold ENPs, CO_2 gas undergoes no coagulation and deposition processes; thus, it is an ideal candidate for verifying the mix. If well-mixed conditions are achieved, the real-time CO_2 volume inside the chamber is expressed as follows:

$$\frac{dc_u(t)}{dt} = \frac{F_0 c_0 + F_1 c_1 - F_2 c_u(t)}{V} \tag{17}$$

where $c_u(t)$ is the CO_2 volume at time t for the zone 1 chamber and c_0 and c_1 are the CO_2 volume in the pure CO_2 cylinder and air, respectively. In this study, $c_0 = 1$, and $c_1 = 0.0143$. An analytical solution for Eq. (8) can be easily obtained using

$$c_u(t) = e^{-F_2 t}(c_1 - A) + A \tag{18}$$

Where $A = \frac{F_0 c_0 + F_1 c_1}{F_2}$. In theory, the well-mixed conditions are considered achieved if the measured CO_2 volume fits the analytical results obtained using Eq. (18).

For the experiment, the CO_2 injection start time in zone 1 was 270 s because the continuous injection lasts 845 s. Pure air was then continuously injected into the chamber, with a flow rate 4.5 lpm. The analytical solution shown in Eq. (18) was used as a reference to validate the experiment, as shown in Fig. 2. The sample was measured using the OneLine3020 ABB instrument. The total measurement time lasted for more than 6 h. The experimental results and theoretical model only slightly deviated for the zone I chamber throughout the experimental process. The experimental solution and analytical solution overlapped during the injecting process, indicating that the well-mixed condition was achieved in the zone I test chamber. ENPs have nearly the same transport properties as do gases because of their small Stokes number, regardless of the material; thus, the well-mixed conditions in the zone I chamber are also suited for gold ENPs.

3.2. Characteristics of the sourced gold ENPs

Fig. 3 shows the TEMs of gold ENPs generated using a spark discharge generator. The gold ENPs were captured using a low-pressure impactor. The results indicated fractal-like properties of the generated gold ENPs, as reported in [27,45]. Investigating the gold ENP dynamics requires introducing the fractal theory to characterize the particle transport property. The key to this achievement is specifying the gold ENP fractal dimension and primary particle size. This study assumed that the statistical fractal dimension of gold ENPs was 1.75, as in the previous study [17], which is in close agreement with simulated structures from diffusion-limited cluster aggregation for gold aggregates, approximately 1.8 [44]. The primary particle diameter was approximately 5 nm, which is consistent with Tabrizi et al.'s finding obtained using nearly the same equipment and carrier gas, N_2 [27].

The PSD $s(v,t)$ for the source and deposition loss rate coefficient $\lambda_d(v)$ must be specified before performing PBM. Because of measurement errors and source instabilities, the measured gold ENP size distributions are not absolutely identical, even between two consequent measurements, as shown in Fig. 4. Thus, using only one measurement as the model input is forbidden. In this study, we used three measured data for the source before the experiment and three measured data after the experiment as multiple basis data and subsequently used the least square approximation (LSA) method to obtain a fitted size distribution for the source. Fig. 4 shows that the measured data for the source before and after the experiment (the duration exceeded 2 h) very well fit to each other, indicating that the source by spark discharge is steady.

We proposed the following method for fitting the measured data. On the basis of the measurements, the PSD was first assumed to follow a log-normal distribution

$$n^e(\ln d_m) = \frac{N_t}{(2\pi)^{1/2}\ln\sigma_g} \exp\left(-\frac{(\ln d_m - \ln\overline{d_{mg}})^2}{2\ln^2\sigma_g}\right) \tag{19}$$

where d_m is the particle diameter, $N_t$is the total particle number, $\sigma_g$is the geometric standard deviation (GSD) for the number size distribution, and $\overline{d_{mg}}$ is the geometric mean diameter (GMD). This assumption was valid for almost all sources [8]. Eq. (19) was further simplified by considering the natural logarithm,

$$\ln(n^e) = \ln(N_t) - \ln\left((2\pi)^{\frac{1}{2}}\ln\sigma_g\right) - \frac{(\ln d_P - \ln\overline{d_{mg}})^2}{2\ln^2\sigma_g} \tag{20}$$

The GMD, $\overline{d_{mg}}$, can be easily determined from the measurements, and the next task is to determine the total particle number, N_t, and GSD, σ_g , by using a common LSA method. The same procedure yielded the curve fitted to multiple measured sources shown in Fig. 4. The source measurement was performed six times both before and after the injection. The source was stable within a reasonable range for experimental errors and can thus be considered ideal for this study. According to the log-normal distribution theory, the source properties were characterized using three key quantities, namely the total particle number concentration (N_0), GSD for the number size distribution, and GMD. For implementing PBM, the mobility diameter, shown in Fig. 4, must be converted to the equivalent diameter of the aggregate.

3.3. Deposition loss rate coefficient

Particle loss because of deposition during the test chamber aerosol dynamics studies is an unavoidable dynamical process [19,33]. Two ideal methods, namely the least square approximation (LSA) method [19] and averaged method (AM) [25], were proposed to identify the size-dependent deposition rate coefficients. Both methods have similar measured data requirements; briefly the total particle number must be below a certain value, typically 1.0×10^4 #/cm^3, which allows disregarding coagulation-induced particle loss. To meet this requirement, we selected a measurement with a total particle number below 1.0×10^4 #/cm^3 to obtain the deposition loss rate coefficient. In this study, we used the AM, as shown in Fig. 5. This figure presents the deposition loss rate coefficient and deposition velocities for different surfaces on the basis of Lai and Nazaroff's theoretical model (2000) for comparison. The friction velocity for the theoretical model was 8.0 cm/s. For diameters ranging from 40 to 200 nm, the deposition loss rate coefficients obtained using the AM fit those obtained using Lai and Nazaroff's theoretical model [33]. The same conclusion was obtained using the same fan speed with a single-zone chamber.

Table 1
Experimental parameters.

Source			Ventilation rate (lpm)	Chamber	Deposition Friction velocity	SMPS parameters		Air temperature (K)
TPC(#/cm^2)	GMD (nm)	GSD				Size range (nm)	Qsh/Qs (lpm)	
6.37e7	28.9	1.63	4.0	$1 \times 1 \times 1$ m^3	8 cm/s	5.94–224.7	15/1.45	297

These results indicate the reliability of the deposition loss rate coefficient obtained from the AM for the zone 1 chamber. PBM requires Lai and Nazaroff's theoretical Eq. (5), with a friction velocity of 8.0 cm/s as the input.

3.4. Gold ENP evolution measured by SMPS3936

Table 1 summarizes the experimental parameters used in this study. In the experiment, gold ENPs generated using a spark discharge generator were injected into the zone I chamber with nitrogen, at a flow rate of 4.0 lpm. The source injection into the test chamber lasted for 3.975 h. Before and after the injection, we used SMPS3936 to measure the size distribution, as shown in Fig. 4. Similar to that in a previous study [8], the size distribution of the gold ENPs, as shown in Fig. 6, exhibits a bimodal distribution during injection The primary mode quickly reached a steady state; briefly, the diameter and magnitude of the mode did not change over time. In addition, an interesting characteristic of the primary mode was determined. The magnitude first increased to a maximum value before decreasing to its steady state; briefly, both magnitude and mode size remained constant during the injection. A similar observation was reported by Seipenbusch et al. [8] for platinum ENPs; however, the dependent factors remain poorly illustrated. In the secondary mode, the diameter increased, while the magnitude decreased with time on its first emergence because of the coagulation mechanism. An interesting discovery for the secondary mode was observed because the secondary mode nearly followed a line with a fixed slope on emerging.

3.5. Comparison between the experiment and PBMs

This section compares the size-resolved evolution of aggregate size distribution between the measurement and model. The mass equivalent size, which was used as an internal coordinate of the aggregate number function, as shown in Eq. (4), was converted to the mobility diameter for conducting a comparative study of experiments and simulations. The conversion from mass equipment size to mobility for all PBMs was performed using Eq. (2) given the comparative study among different PBMs and the measurement by TSI SMPS 3936 [30].

To implement PBM, several input parameters, including the aggregate source size distribution, ventilation flow rate, aggregate deposition loss rate, aggregate primary particle size, aggregate fractal dimension, and air atmospheric temperature, needs to be specified or measured beforehand [17]. In this study, the particle source size distribution and deposition loss rate in PBM were identical to the measurements, as shown in Figs. 4 and 5, respectively. The ventilation flow rate through the chamber was 4.0 lpm, which was identical to the measurement implemented using an electrical flowmeter. This ensures the implementation of the experiment and simulation under the same condition. As the moving SM was used in PBM, the bin number was 300 with a space factor of 1.13, which ensures the accuracy of this method considering numerical calculations. Table 2 shows some key parameters used in the PBM.

As discussed in Section 2.2.3, four representative aggregate collision models were used for implementing PBM in this study, namely the modified Fuchs collision model [34], Dahneke's transition regime collision model [23], harmonic mean collision model, and model for all diffusive Knudsen numbers developed by Thajudeen et al. [35] Fig. 7(a) compares the plots for both measured and modeled size distribution evolution, whereas Fig. 7(b) presents the total particle number. Notably, PBM with the harmonic mean aggregate collision kernel is not presented in Fig. 7(a) because it nearly overlapped with the Dahneke's collision function. Fig. 7(a) shows all PBM considering that different aggregate coagulation kernels produce highly similar patterns of PSD over time to the experiment, in which two modes exist. At 32×135 s, the experiment showed that the first mode has been in a steady state because its characteristic quantity, including the particle number and diameter, changed negligibly over time. Our simulation showed that only PBM with the Thajudeen et al.'s aggregate function [35] successfully captured this characteristic of PSD over time; whereas for that with modified Fuchs collision rate function [34] and Dahneke's collision function [23], the first model was in the evolving process until 32×135 s. This indicated their failure to capture the time required to reach a steady state. For the measured first mode at the steady state, the aggregate diameter was 26 nm, and the particle number was 1.45×10^6#/cm^3. However, for the simulated mode by using the Thajudeen et al.'s aggregate function, the aggregate diameter was 34 nm, and the particle number was 1.30×10^6#/cm^3. Therefore, the relative errors of simulated data for the first mode diameter and mode number to the measurement were approximately 30% and 10%, respectively. PBM with the modified Fuchs collision rate function and Dahneke's collision function inevitably resulted in much larger relative errors to the measurement for the two characteristic quantities, exceeding approximately 40% and 50%, respectively. Notably, for the secondary mode, the measurement showed a slope over time until disappearance. PBM with the Thajudeen et al.'s aggregate function successfully captured the evolution of the secondary mode; particularly, both simulation and measurement yielded the same slope value for the slopes. PBM with the modified Fuchs collision rate function and Dahneke's collision function yielded nearly the same slopes but were apparently different from the measurement and PBM with the Thajudeen et al.'s aggregate function. Overall, PBM with the Thajudeen et al.'s aggregate function yielded the nearest PSD with the measurement among all investigated aggregate collision functions; particularly, it can capture all key characteristics of PSD over time with high accuracy. PBM with the modified Fuchs collision rate function, Dahneke's collision function, and harmonic mean collision function could not capture the time of the PM approaching the steady state and did not yield an appropriate slope of the secondary mode.

When a steady source is continuously injected into a chamber, the measurement using the SMPS 3936 showed that the total aggregate number first increased to a maximum and then slowly decreased, finally to a steady state, as shown in Fig. 7(b). All PBM in this study captured the same evolution of the total aggregate number as the measurement; however, only the PBM with the Thajudeen et al.'s aggregate function fit well to the quantitative measurement. We observed favorable agreement between the measurement and PBM with the Thajudeen et al.'s aggregate collision function, indicating that this method can trace the evolution of the total aggregate number over time. Here, we calculated the relative errors of simulations to the measurement at 3.5 h for calculating the total aggregate number, namely 12.5% for PBM with

Table 2
Parameters in the implementation of PBM.

Source			Ventilation rate (lpm)	Chamber (m^3)	Friction velocity	Aggregate			Air temperature (K)	Gold density (kg/m^3)	Bin number	Time step (s)
TPC (cm^{-3})	GMD (nm)	GSD				Primary particle diameter (nm)	Fractal dimension	Pre-exponential factor				
6.37e7	28.9	1.63	4.0	1	8 cm/s	5	1.75	1.30	297	19600	300	27

the Thajudeen et al.'s aggregate collision function, 65% for PBM with the modified Fuchs collision function, and 55% for PBM with the Dahneke collision function and harmonic mean collision function.

In summary, PBM with the Thajudeen et al.'s aggregate collision function showed apparent advantage in accuracy compared with other collision functions for capturing both evolution of detailed PSD and the statistical aggregate number. This method can yield the nearest PSD as the measurement over time and provide the total aggregate number with relative errors to the measurement smaller than 12.5%, indicating that the Thajudeen et al.'s aggregate collision function should be employed in PBM because highly accurate simulation is required. Note that in Fig. 7(a), Eq. (2) was used to relate aggregate mobility diameter to mass equipment diameter for all aggregation functions. As Eq. (12) was used to relate aggregate mobility diameter to mass equipment diameter for the Thajudeen et al.'s aggregate collision function, much smaller relative errors of the PBM to the measurement is expected.

3.6. Reliability of PBM with the Thajudeen et al.'s aggregate collision function

In contrast to particle tracking methods, such as Langevin simulation where each aggregate's shape can be characterized, for implementing PBM, as discussed in Section 3.5, the input fractal dimension (D_f), pre-exponential factor (k_f), and primary particle diameter (d_{p0}) were assumed as constants over time (1.75, 1.30, and 5 nm, respectively). However, the specification of these parameters are not arbitrary because the fractal dimension and primary particle diameter are from the statistics based on the TEM data discussed in Section 3.2, whereas the pre-exponential factor was obtained from the study by Thajudeen et al. [35] Researchers, such as Heinson et al. [10,10] have extensively shown that the pre-exponential factor is not a constant during aggregation, and this factor is not the same for all aggregates in any population. The same problem occurs for the fractal dimension. The challenge was subsequently evaluated for validating PBM with the specified constants D_f, k_f, and d_{p0}.

Fig. 7 shows the effect of the pre-exponential factor on the size distribution evolution over time (Fig. 7(a)), and the total particle number (Fig. 7(b)) is presented as different pre-exponential factors (i.e., 1.0, 1.3, 1.6, and 1.9). The results revealed that the pre-exponential factor did not apparently affect detailed PSD and total aggregate number, indicating that this factor is not a key parameter determining the accuracy of PBM for studying aggregate evolution over time. The effect of the fractal dimension on the aggregate size distribution and total aggregate number over time was investigated as the fractal dimension specified as 1.55, 1.75, 2.4 and 3.0 (Fig. 8). High agreement was observed between PBM and the measurement only at D_f =1.75, which is a statistical value from TEM measurements discussed in Section 3.2 and is also in close agreement with simulated structures from diffusion-limited cluster aggregation for gold aggregates, approximately 1.8 [44]. The over-predicted total aggregate number for D_f exceeded 1.75, whereas an underpredicted total aggregate number for D_f was smaller than 1.75. As the fractal dimension was 3.0, the relative error of PBM to the measurement at 3.5 h was even up to 256%, indicating that the fractal dimension is a key parameter affecting the accuracy of PBM. Thus, it should be appropriately specified beforehand. Fig. 9 shows the comparison of detailed PSD (Fig. 9 (a)) and total aggregate number (Fig. 9(b)) over time, with different primary particle diameters for PBM. At the primary particle diameter of 5 nm, high agreement can be achieved between PBM and the measurement. Larger deviation occurred between PBM and the measurement when the specified primary particle diameter was larger or smaller than 5 nm. It indicated that in addition to the fractal dimension, the primary particle diameter is another key parameter affecting the accuracy of PBM, which must be appropriately specified before implementing PBM.

4. Discussion

PBM is feasible mathematically, particularly when the PBE is solved through the highly size-resolved SM. Modern mathematical techniques, such as the fourth-order Runge–Kutta method, can adequately ensure accurate ODE solutions, regardless of whether the PBE is solved through the SM, MOM, or Monte Carlo method [46]. However, some uncertain input parameters or formulae exist, which must be specified or selected by users before implementing PBM, such as the aggregate collision kernel, aggregate fractal dimension, diffusion coefficient and pre-exponential factor [37,47,48]. These uncertain factors inevitably lead to deviations between PBM and realities, particularly for size-resolved PSD during evolution, which has received attention by scientists for investigating the effect of workplace ENPs on human health [8]. Thus, a question arises, does the PBM provide realistically resolved information on PSD over time for fractal-like ENPs and to what extent does PBM agree with real physics versus only being a numerical solution, particularly under realistic high concentration where the rapid change of PSD occurs? These questions motivated the present study. The coupling between Navier-Stokes equations for flow field and governing equations for dispersed phase has become a major method for studying particle-laden multiphase flow [49,50], however, the solution of Navier-Stokes equation as well as its coupling with the PBE was deliberately avoided to achieve a quantitative comparison of the evolving PSD between the PBM and measured data under an ideal condition.

In this study, a chamber ENP dynamics involving ENP production, deposition, coagulation, and transport was designed at Karlsruhe Institute of Technology, Germany, to develop aerosol dynamics processes under realistic scenarios. The experiment was divided into four parts; each part fulfilled one task. all parts aimed at achieving the study target. In part I, we focused on the sourced particle characterization, including the specification of the fractal dimension and primary particle diameter based on the TEM data (Fig. 3) and the sourced aggregate PSD measured using SMPS 3936 (Fig. 4), which completely determined the success or failure of the further implementation of PBM. To ensure the steady state of the source, we carefully checked the sourced PSDs before and after the injection for several hours and verified that our spark discharge generator generated steady sources during the experiment. To maximally reduce the measurement errors, we proposed

a novel least square method to fit the measurement for the soured PSD before and after the injection, as shown in Fig. 2, which was used as an input while implementing the PBM. In part II, we used a tracer gas (i.e., CO_2) to assess whether a well-mixing assumption can be used for our test chamber; if it could be used, the PBE shown in Fig. 4 is valid, otherwise the following comparison between the simulation and measurement is invalid. In this part, we verified the feasibility of the well-mixing assumption for the tracer gas (Fig. 2). We further deduced that the well-mixing assumption is valid for gold ENPs investigated in this study because of its very small Stokes number. Moreover, in part III, we designed an experiment with the total particle number of less than $1 \times 10^4 \#/cm^3$ [25] under the case our recently proposed average method was performed to determine the aggregate deposition loss rate. The experiment for implementing the comparison between the measurement and simulation was conducted in part IV, in which the steady source, shown in Fig. 4, was continuously injected into the chamber for 3.975 h. Fig. 6 shows the measured PSD over time by using SMPS 3936, which was further used as a reference to validate PBM. In total, every session of the experiment, which might affect the accuracy of PBM has been carefully considered and appropriately dealt with, thus ensuring the final comparative study on the PSD over time between PBM and the measurement under a reasonable condition with the least possible uncertain factors.

Once released into the gas environment under realistic scenarios, ENPs undergo several physical changes over a distance from an NP source [8]. The physical changes involve production from a source or sources, coagulation, deposition, and transport through ventilation; these physical changes solitarily or in combination change the PSD of ENPs over time and distance. Thus, the challenge of PBM, which is determined on the basis of the PBE shown in Eq. (4), captures the evolution of the PSD of ENPs by considering all relevant physical changes or dynamics. It requires all physical changes to be appropriately considered using the corresponding models in the PBE. Under the simulated scenarios investigated in this study, the reliability of models for the aggregate production, deposition, and transport can be high according to reliable measurements as well as relevant theoretical analysis. As discussed in Section 3.2, the production rate for ENPs was determined with high reliability by using SMPS 3936 and the least square approximate technique. In Section 3.3, the deposition rate considering the aggregate mobility diameter was obtained according to the analysis of the data measured by using the newly developed AM. Studies have performed a similar procedure for achieving the deposition rate in a closed chamber [19,51]. For the transport, ENPs can be considered to have a velocity same as their surrounding gas because of very small Stokes number and thus can be easily measured using a highly accurate flowmeter. Thus, the key doubt regarding the reliability of PBM should attribute to coagulation. Notably, the aggregate collision rate coefficient remains ambiguous [35]. In addition, some assumptions while implementing PBM, namely D_f, k_f, and d_{p0}, specified as constants, increases the feasibility of PBM by two-folds for resolving the problem. Therefore, in this study, we focused on the validation of PBM with a suitable aggregate collision kernel. Four representative aggregate collision rates were investigated, namely the modified Fuchs collision model [34], Dahneke's transition regime collision model [23], harmonic mean collision model, and model for all diffusive Knudsen numbers developed by Thajudeen et al. [35]. Fig. 7 shows that PBM with the aggregate collision function, i.e. Thajudeen et al.'s coagulation kernel, produces the nearest PSD to the measurement under the same condition and particularly captures the evolution of two modes of the PSD. More importantly, PBM with this aggregate function highly agrees with the measurement of the total aggregate number. This confirmed that PBM can provide real information on the PSD of ENPs during evolution. Especially, as the Thajudeen et al.'s aggregation kernel is employed in the implementation of PBM, the accuracy of PBMs, such as nanoparticle synthesis in combustion flow [52] and soot dynamics [53],is expected to be increased significantly. We further investigated the effect of D_f, k_f, and d_{p0} on the accuracy of PBM (Figs. 8–10) and observed that PBM shows the maximum agreement with the measurement when these parameters are specified according to the measurement and previously reported suggestions [35]. In the Thajudeen et al.'s aggregation kernel, a more reasonable definition of particle mobility size in terms of the particle's mass equipment size was proposed. It is expected the accuracy of modified Fuchs collision model [34], Dahneke's transition regime collision model [23], and harmonic mean collision model can be improved as the Thajudeen et al.'s definition for the mobility diameter is introduced.

5. Conclusion

An experiment was artificially designed in a simulated chamber to verify the reliability of PBM for studying the PSD of fractal-like ENPs under realistic high concentration, and crucial factors affecting the accuracy of this method. Gold ENPs with a primary particle diameter of 5 nm and aggregate fractal dimension of 1.75 were generated using a self-made spark discharge generator, which was used as the source in the experiment. The well-mixing condition of the simulated chamber was verified by detecting the real-time carbon dioxide volume by using the OneLine3020 ABB instrument. The deposition loss rate coefficient was determined using our developed AM, which provides the friction velocity as input parameters in the deposition model [33]. During the experiment, the aggregate number considering the mobility diameter was measured using TSI SMPS 3936. The PBE involving the same physical changes in aggregates as those in the experiment was established, which was further solved using the moving SM. The solution of the PBE was highly ensured considering its small numerical time, 27 s, and a small bin space factor, 1.13. The modified Fuchs collision rate function, Dahneke's collision function, harmonic mean collision function, and the aggregate function newly developed by Thajudeen et al. were used for implementing PBM.

A comparative study was conducted on an aerosol process between the measurement and PBM, in which a steady source was continuously injected into the simulated chamber. We observed that PBM with the Thajudeen et al.'s aggregate function apparently had a higher accuracy than did other aggregate collision rates, and the relative errors of PBM to the measurement for the total aggregate concentration was only 12.5% when the steady state was reached. Thus, PBM with the Thajudeen et al.'s aggregate function was verified as the most reliable method for studying fractal-like ENP dynamics. When implementing PBM with this aggregate function, two key parameters, namely the fractal dimension and primary diameter, played a crucial role in determining the accuracy of PBM. Thus, these two parameters were recommended to be specified according to the analysis of the TEM data. Although the pre-exponential factor was also considered crucial in characterizing aggregate shape, it was found it only slightly affected the accuracy of PBM for studying the PSD of fractal-like ENPs. The study finally verified the PBM with constant fractal dimension, primary diameter and pre-exponential factor is valid for investigating the size-resolved evolution of ENPs over time, although these parameters might vary during evolution.

Acknowledgments

The authors thank Mr. Santiago Onel at Karlsruhe Institute of Technology for the TEM measurements of the gold ENPs. Dr. Yu thanks the Alexander von Humboldt Foundation (grant no.

1136169) and the Sino-German research project (GZ971). Moreover, the authors thank the joint support from the National Natural Science Foundation of China (grant nos. 11372299 and 11632016).

References

[1] B. Buesser, S.E. Pratsinis, Design of nanomaterial synthesis by aerosol processes, Annu. Rev. Chem. Biomol. Eng. 3 (2012) 103–127, http://dx.doi.org/10.1146/annurev-chembioeng-062011-080930.

[2] V. Raman, R.O. Fox, Modeling of fine-particle formation in turbulent flames, Annu. Rev. Fluid Mech. 48 (2016) 159–190, http://dx.doi.org/10.1146/annurev-fluid-122414-034306.

[3] A. Moiseev, F. Qi, J. Deubener, A. Weber, Photocatalytic activity of nanostructured titanium dioxide from diffusion flame synthesis, Chem. Eng. J. 170 (2011) 308–315, http://dx.doi.org/10.1016/j.cej.2011.03.057.

[4] S.K. Friedlander, Smoke, Dust and Haze: Fundamentals of Aerosol Behavior, 2nd Ed., John Wiley & Sons Inc, 2000, http://adsabs.harvard.edu/abs/1977wiEllipsisbookEllipsis.F.

[5] M. Sgraja, J. Bloemer, J. Bertling, P.J. Jansens, Experimental and theoretical investigations of the coating of capsules with titanium dioxide, Chem. Eng. J. 160 (2010) 351–362, http://dx.doi.org/10.1016/j.cej.2010.02.061.

[6] H.Y. Sohn, S. Perez-Fontes, J.W. Choi, Computational fluid dynamic modeling of a chemical vapor synthesis process for aluminum nanopowder as a hydrogen storage precursor, Chem. Eng. J. 156 (2010) 215–225, http://dx.doi.org/10.1016/j.cej.2009.10.044.

[7] M. Petitti, M. Vanni, D.L. Marchisio, A. Buffo, F. Podenzani, Simulation of coalescence, break-up and mass transfer in a gas-liquid stirred tank with CQMOM, Chem. Eng. J. 228 (2013) 1182–1194, http://dx.doi.org/10.1016/j.cej.2013.05.047.

[8] M. Seipenbusch, A. Binder, G. Kasper, Temporal evolution of nanoparticle aerosols in workplace exposure, Ann. Occup. Hyg. 52 (2008) 707–716, http://dx.doi.org/10.1093/annhyg/men067.

[9] T. Thajudeen, R. Gopalakrishnan, C.J. Hogan, The collision rate of nonspherical particles and aggregates for all diffusive Knudsen numbers, Aerosol Sci. Technol. 46 (2012) 1174–1186, http://dx.doi.org/10.1080/02786826.2012.701353.

[10] W.R. Heinson, C.M. Sorensen, A. Chakrabarti, Does shape anisotropy control the fractal dimension in diffusion-limited cluster-cluster aggregation?, Aerosol Sci Technol. 44 (2010) i–iv, http://dx.doi.org/10.1080/02786826.2010.516032.

[11] M. von Smoluchowski, Versuch einer mathematischen Theorie der Koagulationskinetik kolloider L{ö}sungen, Z. Phys. Chem. 92 (1917) 129–168.

[12] C.G.R. Nazaro, W. William, Mathematical modeling of indoor aerosol dynamics, Environ. Sci. Technol. 23 (1984) 157–166.

[13] X. Woo, R. Tan, Simulation of mixing effects in antisolvent crystallization using a coupled CFD-PDF-PBE approach, Cryst. Growth Des. 6 (2006) 1291–1303. http://pubs.acs.org/doi/abs/10.1021/cg0503090 (accessed August 12, 2013).

[14] M. Yu, Y. Liu, J. Lin, M. Seipenbusch, Generalized TEMOM scheme for solving the population balance equation, Aerosol Sci. Technol. 49 (2015) 1021–1036, http://dx.doi.org/10.1080/02786826.2015.1093598.

[15] E. Otto, H. Fissan, S. Park, K. Lee, Log-normal size distribution theory of Brownian aerosol coagulation for the entire particle size range: Part II—analytical solution using Dahneke's coagulation kernel, J. Aerosol Sci. 30 (1999) 17–34.

[16] W. Qinglan, NANOTRANSPORT-Project, http://cordis.europa.eu/pub/nanotechnology/docs/nanotransport_quinglan_wu.pdf, 2006.

[17] S. Anand, Y.S. Mayya, M. Yu, M. Seipenbusch, G. Kasper, A numerical study of coagulation of nanoparticle aerosols injected continuously into a large, well stirred chamber, J. Aerosol Sci. 52 (2012) 18–32, http://dx.doi.org/10.1016/j.jaerosci.2012.04.010.

[18] D. Rim, J.-I. Choi, L.A. Wallace, Size-resolved source emission rates of indoor ultrafine particles considering coagulation, Environ. Sci. Technol. 50 (2016) 10031–10038, http://dx.doi.org/10.1021/acs.est.6b00165.

[19] T. Hussein, A. Hruška, P. Dohányosová, L. Džumbová, J. Hemerka, M. Kulmala, et al., Deposition rates on smooth surfaces and coagulation of aerosol particles inside a test chamber, Atmos. Environ. 43 (2009) 905–914, http://dx.doi.org/10.1016/j.atmosenv.2008.10.059.

[20] C. He, L. Morawska, L. Taplin, Particles emission characteristic of office printers, Environ. Sci. Technol. 41 (2007) 6039–6045.

[21] N.A. Fuchs, The Mechanics of Aerosols, Dover Publications, 1964.

[22] J.H. Seinfeld, S.N. Pandis, Atmospheric Chemistry and Physics: From Air Pollution to Climate Change, John Wiley & Sons, 2012.

[23] B. Dahneke, Simple kinetic theory of Brownian diffusion in vapors and aerosols, Theory Dispersed Multiph. Flow. 2 (1983) 97–133.

[24] A. Joonas Koivisto, M. Yu, K. Hämeri, M. Seipenbusch, Size resolved particle emission rates from an evolving indoor aerosol system, J. Aerosol Sci. 47 (2012) 58–69, http://dx.doi.org/10.1016/j.jaerosci.2011.12.007.

[25] M. Yu, A.J. Koivisto, K. Hämeri, M. Seipenbusch, Size dependence of the ratio of aerosol coagulation to deposition rates for indoor aerosols, Aerosol Sci. Technol. 47 (2013) 427–434, http://dx.doi.org/10.1080/02786826.2012.759640.

[26] S. Schwyn, E. Garwin, A. Schmidt-Ott, Aerosol generation by spark discharge, J. Aerosol Sci. 19 (1988) 639–642.

[27] N.S. Tabrizi, M. Ullmann, V.A. Vons, U. Lafont, A. Schmidt-Ott, Generation of nanoparticles by spark discharge, J. Nanopart. Res. 11 (2008) 315–332, http://dx.doi.org/10.1007/s11051-008-9407-y.

[28] P. DeCarlo, J. Slowik, D.R. Worsnop, P. Davidovits, J. Jimenez, Particle morphology and density characterization by combined mobility and aerodynamic diameter measurements. Part 1: Theory, Aerosol Sci. Technol. 38 (2004) 1185–1205, http://dx.doi.org/10.1080/02786826.2004.10399462.

[29] A.A. Lall, M. Seipenbusch, W. Rong, S.K. Friedlander, On-line measurement of ultrafine aggregate surface area and volume distributions by electrical mobility analysis: II. Comparison of measurements and theory, J. Aerosol Sci. 37 (2006) 272–282, http://dx.doi.org/10.1016/j.jaerosci.2006.01.006.

[30] TSI, Scanning Mobility Particle Sizer – Spectrometer Nanoparticle Aggregate Mobility Analysis Software Module, 2006.

[31] M.D. Allen, O.G. Raabe, Slip correction measurements of spherical solid aerosol particles in an improved millikan apparatus, Aerosol Sci. Technol. 4 (1985) 269–286, http://dx.doi.org/10.1080/02786828508959055.

[32] H. Müller, Zur allgemeinen Theorie ser raschen Koagulation, Fortschrittsberichte {ü}ber Kolloide Und Polym. 27 (1928) 223–250.

[33] A.C.K. Lai, W.W. Nazaroff, Modeling indoor particle deposition from turbulent flow onto smooth surfaces, J. Aerosol Sci. 31 (2000) 463–476.

[34] D.-H. Kim, M. Gautam, D. Gera, Modeling nucleation and coagulation modes in the formation of particulate matter inside a turbulent exhaust plume of a diesel engine, J. Colloid Interface Sci. 249 (2002) 96–103, http://dx.doi.org/10.1006/jcis.2002.8264.

[35] T. Thajudeen, R. Gopalakrishnan, C.J. Hogan Jr., The collision rate of nonspherical particles and aggregates for all diffusive Knudsen numbers, Aerosol Sci. Technol. 46 (2012) 1174–1186.

[36] K. Cho, K.-S. Chung, P. Biswas, Coagulation coefficient of agglomerates with different fractal dimensions, Aerosol Sci. Technol. 45 (2011) 740–743, http://dx.doi.org/10.1080/02786826.2011.558530.

[37] E. Goudeli, M.L. Eggersdorfer, S.E. Pratsinis, Coagulation-agglomeration of fractal-like particles: structure and self-preserving size distribution, Langmuir 31 (2015) 1320–1327.

[38] E. Otto, H. Fissan, S. Park, K. Lee, Log-normal size distribution theory of brownian aerosol coagulation for the entire particle size range: part II–analytical solution using Dahneke's coagulation kernel, J. Aerosol Sci. 30 (1999) 17–34. http://www.sciencedirect.com/science/article/pii/S002185029800038X (accessed April 13, 2012).

[39] S.H. Park, K.W. Lee, E. Otto, H. Fissan, The log-normal size distribution theory of Brownian aerosol coagulation for the entire particle size range Part I — analytical solution using the harmonic mean coagulation kernel, Science 80 (30) (1999) 3–16.

[40] R. Gopalakrishnan, P.H. McMurry, C.J. Hogan, The electrical mobilities and scalar friction factors of modest-to-high aspect ratio particles in the transition regime, J. Aerosol Sci. 82 (2015) 24–39, http://dx.doi.org/10.1016/j.jaerosci.2015.01.001.

[41] T. Thajudeen, S. Jeon, C.J. Hogan, The mobilities of flame synthesized aggregates/agglomerates in the transition regime, J. Aerosol Sci. 80 (2015) 45–57, http://dx.doi.org/10.1016/j.jaerosci.2014.11.003.

[42] T. Thajudeen, S. Deshmukh, C.J. Hogan Jr, Langevin simulation of aggregate formation in the transition regime, Aerosol Sci. Technol. 49 (2015) 115–125.

[43] C. Zhang, T. Thajudeen, C. Larriba, T.E. Schwartzentruber, C.J. Hogan Jr., Determination of the scalar friction factor for nonspherical particles and aggregates across the entire Knudsen number range by direct simulation Monte Carlo (DSMC), Aerosol Sci. Technol. 46 (2012) 1065–1078, http://dx.doi.org/10.1080/02786826.2012.690543.

[44] E. Dickinson, Structure and rheology of colloidal particle gels: Insight from computer simulation, Adv. Colloid Interface Sci. 199–200 (2013) 114–127, http://dx.doi.org/10.1016/j.cis.2013.07.002.

[45] M.E. Messing, K.A. Dick, L.R. Wallenberg, K. Deppert, Generation of size-selected gold nanoparticles by spark discharge—for growth of epitaxial nanowires, Gold Bull. 42 (2009) 20–26.

[46] D. Ramkrishna, M.R. Singh, Population balance modeling: current status and future prospects, Annu. Rev. Chem. Biomol. Eng. 5 (2014) 123–146.

[47] Y. Sung, V. Raman, R.O. Fox, Large-eddy-simulation-based multiscale modeling of TiO2 nanoparticle synthesis in a turbulent flame reactor using detailed nucleation chemistry, Chem. Eng. Sci. 66 (2011) 4370–4381, http://dx.doi.org/10.1016/j.ces.2011.04.024.

[48] A.J. Gröhn, S.E. Pratsinis, K. Wegner, Fluid-particle dynamics during combustion spray aerosol synthesis of ZrO2, Chem. Eng. J. 191 (2012) 491–502, http://dx.doi.org/10.1016/j.cej.2012.02.093.

[49] K. Luo, F. Wu, S. Yang, J. Fan, Numerical investigation of the time-related properties of solid phase in a 3-D spout-fluid bed, Chem. Eng. J. 267 (2015) 207–220, http://dx.doi.org/10.1016/j.cej.2014.12.064.

[50] R.O. Fox, Large-eddy-simulation tools for multiphase flows, Annu. Rev. Fluid Mech. 44 (2012) 47–76, http://dx.doi.org/10.1146/annurev-fluid-120710-101118.

[51] W.J. Riley, T.E. McKone, A.C.K. Lai, W.W. Nazaroff, Indoor particulate matter of outdoor origin: importance of size-dependent removal mechanisms, Environ. Sci. Technol. 36 (2002) 200–207. http://www.ncbi.nlm.nih.gov/pubmed/11831216.

[52] M. Yu, J. Lin, T. Chan, Effect of precursor loading on non-spherical TiO2 nanoparticle synthesis in a diffusion flame reactor, Chem. Eng. Sci. 63 (2008) 2317–2329, http://dx.doi.org/10.1016/j.ces.2007.11.008.

[53] B. Zhao, Z. Yang, M.V. Johnston, H. Wang, A.S. Wexler, M. Balthasar, et al., Measurement and numerical simulation of soot particle size distribution functions in a laminar premixed ethylene-oxygen-argon flame, Combust. Flame 133 (2003) 173–188, http://dx.doi.org/10.1016/S0010-2180(02)00574-6.